

Magnetic Field Induced the Assembling of Photothermal Evaporator for Efficient Solar-driven Desalination

Mingyu Zhou¹, Peng Han², Guicun Qi², Dali Gao², Hamdy Abdel-Ghafar³, Yuchao Wang¹, and Shengyang Tao¹

¹Dalian University of Technology

²Sinopec Beijing Research Institute of Chemical Industry

³Central Metallurgical Research and Development Institute

May 8, 2023

Abstract

Solar-driven interfacial evaporation is a sustainable and economical technology for fresh water generation. Structural design of photothermal material is an effective strategy to improve the evaporation performance but usually bothered by complicated processes and non-adjustability. Herein, magnetic nanoparticles assembled photothermal evaporator was developed, which showed an adjustable spinal array surface under uniform magnetic field induction. By regulating position in the magnetic field, the desirable surface structures could be uniform at relatively low load density of magnetic nanoparticles to improve light absorption via multiple reflection. Magnetic field induced evaporator could accelerate evaporation to over $1.39 \text{ kg m}^{-3} \text{ h}^{-1}$ under 1-sun illumination, which was 2.8 times that of natural evaporation. After coated by carbon layer, magnetic nanoparticles could overcome the oxidation to realize stable evaporation in long-term desalination. The facile strategy to optimize the surface structure via magnetic field is appropriate for various fields with special requirements on surface structure.

Magnetic Field Induced the Assembling of Photothermal Evaporator for Efficient Solar-driven Desalination

Mingyu Zhou, Peng Han, Guicun Qi, Dali Gao, Hamdy Maamoun Abdel-Ghafar, Yuchao Wang* and Shengyang Tao*

Mr. M. Zhou, Prof. Y. Wang, Prof. S. Tao

State Key Laboratory of Fine Chemicals, Frontier Science Center for Smart Materials Oriented Chemical Engineering, School of Chemical, Dalian University of Technology, Dalian 116024, China E-mail: wangyuchao@dlut.edu.cn; taosy@dlut.edu.cn

Dr. P. Han, Dr. G. Qi, Dr. D. Gao SINOPEC Beijing Research Institute of Chemical Industry, Beijing, 100013, People's Republic of China

Prof. H. M. Abdel-Ghafar

Central Metallurgical Research and Development Institute, P.O. Box: 87, Helwan, 11421 Cairo, Egypt

Keywords: photothermal evaporation, desalination, carbon-coated magnetic nanoparticles, magnetic field induced, adjustable surface structure

Abstract

Solar-driven interfacial evaporation is a sustainable and economical technology for fresh water generation. Structural design of photothermal material is an effective strategy to improve the evaporation performance

but usually bothered by complicated processes and non-adjustability. Herein, magnetic nanoparticles assembled photothermal evaporator was developed, which showed an adjustable spinal array surface under uniform magnetic field induction. By regulating position in the magnetic field, the desirable surface structures could be uniform at relatively low load density of magnetic nanoparticles to improve light absorption via multiple reflection. Magnetic field induced evaporator could accelerate evaporation to over $1.39 \text{ kg m}^{-3} \text{ h}^{-1}$ under 1-sun illumination, which was 2.8 times that of natural evaporation. After coated by carbon layer, magnetic nanoparticles could overcome the oxidation to realize stable evaporation in long-term desalination. The facile strategy to optimize the surface structure via magnetic field is appropriate for various fields with special requirements on surface structure.

1. Introduction

With serious water pollution and the energy-saving demands for water purification, solar-driven evaporation has received extensive attention due to its potential in terms of water, energy, and environmental sustainability,¹⁻⁴ which is widely recognized as a novel desalination technology for solving water resource scarcity issues.⁵⁻⁷ To realize a desirable evaporation efficiency, various kinds of photothermal materials, have been employed to improve the light application thanks to their high absorption of broad-spectrum solar radiation and light-to-heat conversion.⁸⁻¹⁰ Besides the filtering of ideal materials inside the range of dark matter, the logically designed surface structure is also critical for high performance on solar absorption.^{11,12} The rough photothermal surface with a suitable structure can induce the light transfer on microscale to dramatically reduce the diffuse reflection that is the primary type of light loss.^{13,14} For the classic super-black material, thanks to the vertically aligned array structures, carbon nanotube (CNT) achieved approximate complete light absorption in the whole solar spectrum with an absorbance up to 99.97%.¹⁵ Similarly, confining the plasmonic nanoparticles inside the sub-micron hole channels formed a broadband absorber enabling an absorbance around 99% across the wavelengths from 400 nm to 10 μm .¹⁶

Actually, the superior photothermal performance tends to be revealed by a delicate surface structure that is constructed via complicated processing and rigorous preparation conditions, no matter based on top-down etching or bottom-up assembly.¹⁷⁻¹⁹ Besides the high production costs, fragility of the fine structure is another factor to limit the application of efficient light absorbers in photothermal evaporation. To simplify the structure construction, external field effects are introduced to induce the controllable assembly of nanoparticles to form the proposed structure.²⁰⁻²⁴ In particular, magnetic field is considered an ideal tool for applications in structure management,²⁵⁻²⁷ especially in the construction of functional structures with reconfigurable, recoverable and dynamically adjustable.²⁸⁻³⁰ In Jeong's work, Fe_3O_4 nanoparticles were sprayed onto a Si substrate with patterned nickel islands, and attracted by the external magnetic field to form magnetic micropillars.³¹ Besides, some conical micro-tip patterns could be molded with the aid of a magnetic field.³² In Song's work, the mixture of polydimethylsiloxane (PDMS) polymer with magnetic particles was coated onto the substrate and prepared Janus membranes with cacti-spine arrays by magnetic field-assisted molding.³³

In our previous work, magnetic Fe_3O_4 nanoparticles were directly used to assemble the spine arrays as photothermal surface following the effect of magnetic field, which revealed an obvious improvement in light harvesting.³⁴ However, Fe_3O_4 tends to be oxidized in high temperature and high humidity conditions during evaporation. The generated Fe_2O_3 shows a wider band gap indicating the weakening of photothermal performance.³⁵ Additionally, non-uniform magnetic field distribution on the magnet surface induced the formation of an uneven spiny structure, meanwhile, resulting in a relatively high loading density of magnetic nanoparticles to ensure an integrity photothermal layer. Therefore, it is necessary to alleviate the performance degradation caused by the oxidation of Fe_3O_4 and explore the assembly behavior of magnetic nanoparticles at various relative distances.

Based on the above discussion, in this work, we fabricated a magnetic field induced photothermal evaporator assembled by carbon-coated Fe_3O_4 ($\text{Fe}_3\text{O}_4@\text{C}$) nanoparticles, which revealed the adjustable surface structure corresponding to the relative distance to magnet. To improve the stability of magnetic nanoparticles, we synthesized $\text{Fe}_3\text{O}_4@\text{C}$ by a simple one-step method of coating Fe_3O_4 nanoparticles with a layer of carbon

using glucose as the carbon source (Figure 1). The outer carbon layer of $\text{Fe}_3\text{O}_4@\text{C}$ nanoparticles could provide effective protection for the Fe_3O_4 and maintain a stable photothermal performance after the oxidation of magnetic core. At an appropriate relative distance to the magnet, $\text{Fe}_3\text{O}_4@\text{C}$ nanoparticles assembled into a complete and well-distributed photothermal layer with spine arrays at a low load density of 1 mg mm^{-2} (which was 3 mg mm^{-2} in our previous work) (Figure S1). With the optimized surface structure, the $\text{Fe}_3\text{O}_4@\text{C}$ assembled evaporator obviously improved the evaporation rate up to $1.39 \text{ kg m}^{-2}\text{h}^{-1}$ for water and $1.31 \text{ kg m}^{-2}\text{h}^{-1}$ for seawater under 1-sun illumination. During 8 hours of continuous evaporation for seawater and 4 times regeneration, there was less than 4% performance degradation for $\text{Fe}_3\text{O}_4@\text{C}$ assembled evaporator indicating desirable stability. Magnetic field induced adjustable surface structure with spiny arrays is suitable for efficient solar-driven desalination, as well as a universal method for the structure control to satisfy the requirements of other applications in water treatment.

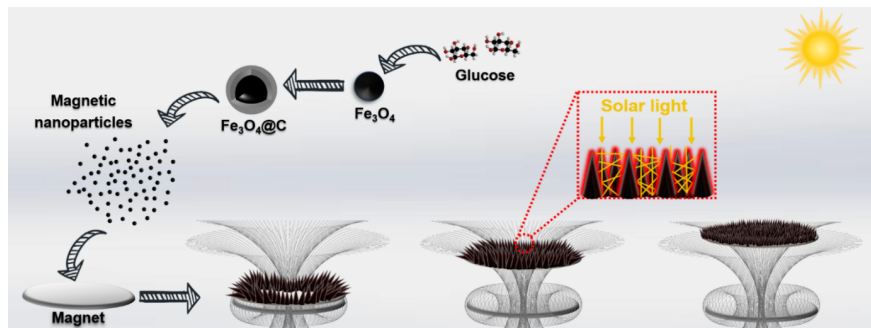


FIGURE 1 Schematic diagram of the synthesis of $\text{Fe}_3\text{O}_4@\text{C}$ and adjustment of the surface structure by controlling relative distance to the magnet. The inserted image shows light reflection inside the spine arrays.

2. Results and Discussion

2.1. Characterization of carbon-coated nanoparticles

The carbon-coated nanoparticles were synthesized by a typical hydrothermal method. After coating with a carbon layer, the carbon-coated nanoparticles remain granular and have a certain dispersion (Figure S2a-b). In the experiment, the thickness of carbon layer was changed by adjusting the amount of glucose as carbon source. As TEM images shown in Figure 2a-c, $\text{Fe}_3\text{O}_4@\text{C}$ had a carbon layer at the thickness of $\sim 15 \text{ nm}$. While, as 2 g of glucose was used in preparation, the thickness of carbon layer of $\text{Fe}_3\text{O}_4@\text{tC}$ was up to $\sim 28 \text{ nm}$. Following the particle size distribution in Figure 2d, the major particle sizes of Fe_3O_4 , $\text{Fe}_3\text{O}_4@\text{C}$ and $\text{Fe}_3\text{O}_4@\text{tC}$ were about 666 nm, 691 nm and 715 nm, respectively. In comparison to the pristine magnetic nanoparticle, $\text{Fe}_3\text{O}_4@\text{C}$ and $\text{Fe}_3\text{O}_4@\text{tC}$ revealed increases in diameter of 25 nm and 49 nm, which were generally consistent with the results in TEM images.

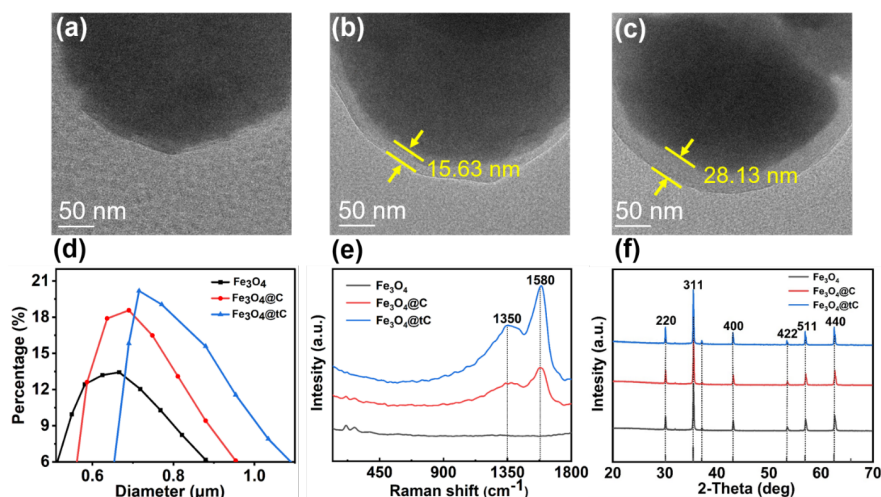


FIGURE 2 TEM images (a-c), particle sizes distributions (d), Raman spectra (e) and XRD spectra (f) of Fe₃O₄, Fe₃O₄@C and Fe₃O₄@tC.

Raman spectra of as-prepared samples were investigated to analysis the carbon layer (Figure 2e). There were two typical D band and G band at 1350 and 1580 cm⁻¹ respectively confirmed in both Fe₃O₄@C and Fe₃O₄@tC, which indicated the relatively low graphitization of the carbon layer.³⁶ In XRD patterns, pristine nanoparticles showed the diffraction peaks at 30, 35, 43, 53, 57 and 63° corresponding to the (220), (311), (400), (422), (511) and (440) of Fe₃O₄ crystal. Fe₃O₄@C and Fe₃O₄@tC showed similar patterns without a noticeable change in these characteristic peaks, indicating no oxidation during the hydrothermal synthesis (Figure 2f).

2.2. Characterization of magnetic photothermal evaporator

The morphology assembled by the magnetic nanoparticles was controlled by the magnetic field. Therefore, the numerical simulation based on finite-element analysis was applied for the analysis of the magnetic field distribution (Figure 3 and Figure S4).

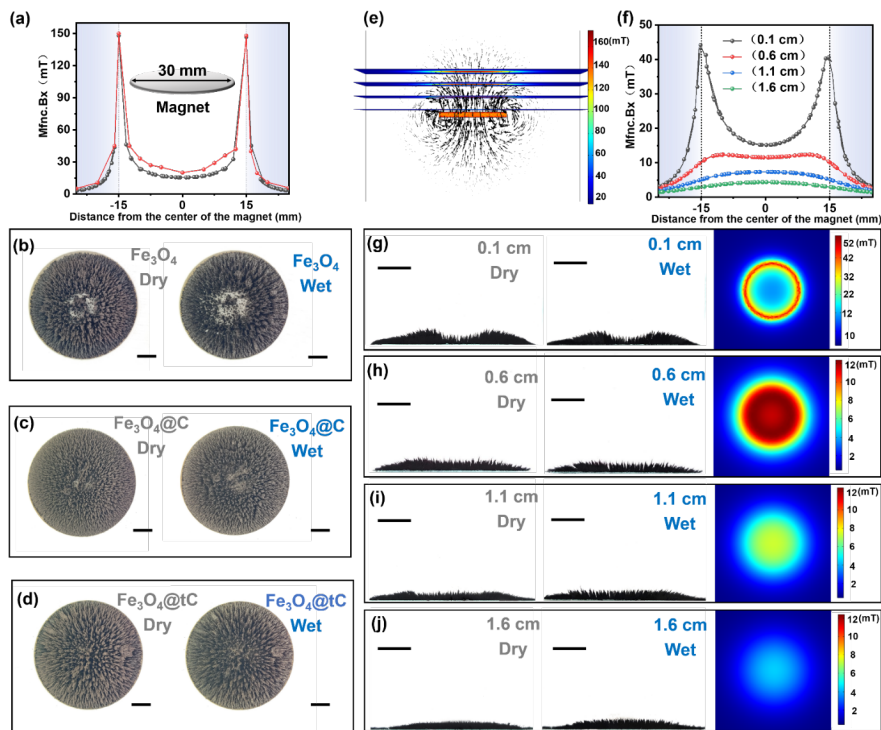


FIGURE 3 The distribution of magnetic field strength at different distances from the center of the magnet in vertical direction (a). The red line and gray line represent the actual measured data and the simulated data respectively. The inserted image is schematic diagram of the magnet with a diameter of 30 mm. Optical photographs of surface morphology on magnetic evaporator before and after wetted by water with Fe_3O_4 (b), $\text{Fe}_3\text{O}_4@\text{C}$ (c) and $\text{Fe}_3\text{O}_4@\text{tC}$ (d) as photothermal materials, respectively. The scale bar was 5 mm. Simulated magnetic field distribution at various distances with the corresponding magnetic field strength (e, f). Spiny morphology of the photothermal layers formed by $\text{Fe}_3\text{O}_4@\text{C}$ at various distances (g-j). The scale bar was 6 mm.

As shown in Figure 3a, the simulated magnetic strength of the magnet edge could reach over 150 mT. While the strength gradually decreased from edge to center down to just ~ 20 mT. Such result was generally consistent with the data from actual measurements (red line in Figure 3a and Figure S5). Because of the non-uniform magnetic field distribution, as the distance between evaporator surface and the magnet below was close (0.1 cm), Fe_3O_4 nanoparticles were preferentially distributed on the edge with stronger magnetic fields. Comparatively, the central region with weaker magnetic field strength exposed the underlying air-laid paper due to fewer magnetic nanoparticles as the loading density of just 1 mg mm^{-2} (Figure 3b).

As Fe_3O_4 was replaced by $\text{Fe}_3\text{O}_4@\text{C}$, spines of the $\text{Fe}_3\text{O}_4@\text{C}$ turned denser and smaller, and tended to form a more well-distributed spiny structure. The exposed region in the center of the magnet was relatively minimized (Figure 3c). It was speculated that the change in the distribution of carbon-coated nanoparticles was attributed to the decrease in magnetic intensity of $\text{Fe}_3\text{O}_4@\text{C}$, which resulted in deviation of the magnetic particle arrangement from the magnetic field (Figure S3). Owing to the weaker magnetic property, $\text{Fe}_3\text{O}_4@\text{tC}$ assembled into fewer spines and covered the magnet surface completely.

During practical solar-driven evaporation, photothermal layer would be wetted by water, and it was necessary to investigate morphology in the wet state. After wetting, the exposed regions of the spiny surfaces composited by Fe_3O_4 and $\text{Fe}_3\text{O}_4@\text{C}$ tended to be larger, and some small spines gathered into larger ones driven by the surface tension of water (Figure 3b-c). However, for $\text{Fe}_3\text{O}_4@\text{tC}$, there was no obvious change in its spiny morphology after wetting (Figure 3d).

As mentioned above, the spiny morphology of photothermal layer was adjustable via controlling the distance between magnetic nanoparticles and magnet. To investigate the effect of distance, the numerical simulation was used to determine the distribution of magnetic fields at four different distances of 0.1 cm, 0.6 cm, 1.1 cm, and 1.6 cm (Figure 3e). The corresponding magnetic field strengths at these distances were shown in Figure 3f. Enlarging the distance to magnet, the magnetic field strength gradually decreased especially at the edge. The magnetic induction intensity of the edge declined from 44 to 11, 6 and 3 mT with the distance increasing from 0.1 to 0.6, 1.1 and 1.6 cm. In comparison, there was a less decline in the center of magnet from 15 to 11, 7 and 4 mT. When the distance from the magnet was 0.6 cm, the magnetic field strength tended to be uniform.

For observing the spine structure conveniently, following the loading density used in this work, a quantity of $\text{Fe}_3\text{O}_4\text{@C}$ nanoparticles was confined in a narrow gap between two glass sheets above the holder with magnet (Figure S6a). As shown in Figure 3g, non-uniform magnetic field distribution caused a denser distribution of $\text{Fe}_3\text{O}_4\text{@C}$ spines at the edge and a relatively sparser spiny structure in the center in both dry and wet states. As the distance increased to 0.6 cm, following the uniform magnetic field, a well-distributed $\text{Fe}_3\text{O}_4\text{@C}$ spines was formed (Figure 3h). However, as the distance got larger to 1.1 and 1.6 cm (Figure 3i-j), the corresponding magnetic field strength became weaker which failed to attract all the $\text{Fe}_3\text{O}_4\text{@C}$ effectively, which caused the less obvious spiny morphology. Similarly, the same trend also existed in the structure composited by Fe_3O_4 (Figure S6b-c).

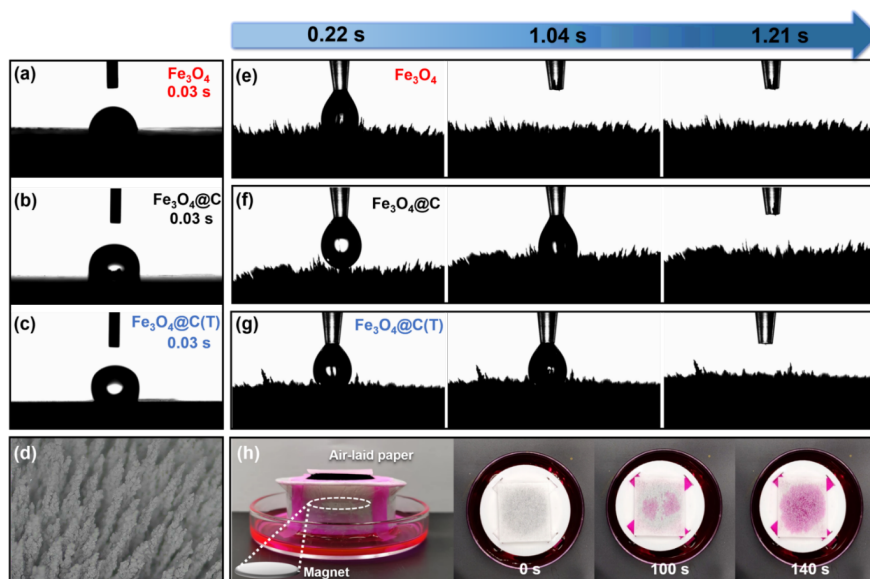


FIGURE 4 Water contact angle images of Fe_3O_4 (a), $\text{Fe}_3\text{O}_4\text{@C}$ (b) and $\text{Fe}_3\text{O}_4\text{@tC}$ (c) after touching 4 μl of water droplet. (d) Microstructure of the photothermal layer formed by $\text{Fe}_3\text{O}_4\text{@C}$. Schematic images of the spiny structures of Fe_3O_4 (e), $\text{Fe}_3\text{O}_4\text{@C}$ (f) and $\text{Fe}_3\text{O}_4\text{@tC}$ (g) contacted with 10 μl of water, the spiny structures could capture water quickly by capillary action. An air-laid paper was laid on the surface of photothermal layer formed by $\text{Fe}_3\text{O}_4\text{@C}$, and tested the water transmission capacity along the photothermal layer (h).

The commercial Fe_3O_4 nanoparticles were hydrophilic, and the hydrophilicity gradually decreased as the carbon layer outside the Fe_3O_4 nanoparticles became thickened (Figure 4a-c). The instantaneous water contact angles of flat surfaces of $\text{Fe}_3\text{O}_4\text{@C}$ and $\text{Fe}_3\text{O}_4\text{@tC}$ were 107.1 and 122.2°, respectively. However, with the spiny structure, all three photothermal surfaces composited by Fe_3O_4 and carbon-coated nanoparticles enabled to capture water in a short time (Figure 4e-g). Figure 4d shows morphology of the photothermal layer formed by $\text{Fe}_3\text{O}_4\text{@C}$ that featured a multi-gap structure with spines. Such structure had capillary channels

all over the interior, which could provide excellent paths for efficient water transport,²³ and water could efficiently transport from the bottom to the top in a short period (about 140 s) by capillary force alone (Figure 4h).

2.3. Light absorptance of magnetic photothermal evaporator

As a fine semiconductor, the band gap of black Fe_3O_4 was just 0.1 eV, and such a quite narrow band gap ensured the nearly full spectrum of solar absorption.³⁷ Under the evaporation environment with high temperature and humidity, Fe_3O_4 is gradually oxidized into Fe_2O_3 which has lower solar-light absorption due to the increase in bandgap.³⁵ In response to this issue, a carbon layer as good light absorber was coated around the magnetic particles to maintain the performance on light harvesting for stable photothermal evaporation. The light harvesting in solar spectrum was carefully investigated based on the UV-vis-NIR spectra in the range of 280–2500 nm.

Without magnetic field, magnetic particles with and without coating were respectively fixed on glass slices to form flat surfaces. As shown in Figure 5a, the diffuse reflectance of $\text{Fe}_3\text{O}_4@\text{C}$ and $\text{Fe}_3\text{O}_4@\text{tC}$ were almost near the result of pristine Fe_3O_4 but with a slight decrease at visible and infrared regions. It indicated that the carbon layer displayed a comparable ability in light absorption to Fe_3O_4 . The diffuse reflectance of $\text{Fe}_3\text{O}_4@\text{C}$ was $\sim 4.4\%$ in UV region (280–400 nm), $\sim 10.1\%$ in visible region (400–780 nm), and $\sim 11.6\%$ in near-infrared region (780–2500 nm). As the nanoparticles assembled into a spiny morphology in magnetic field, there was a significant reduction in diffuse reflection. Fixing the distance to magnet at 0.6 cm, the diffuse reflectance of spiny surface composited by $\text{Fe}_3\text{O}_4@\text{C}$ was down to $\sim 1.6\%$ in UV region, $\sim 5.6\%$ in visible region, and $\sim 6.6\%$ in near-infrared region (Figure 5c). The decrease of diffuse reflectance was attributed to the specific surface microstructure caused by magnetic field. In the gaps of spiny surface, part of the reflected light was re-captured by the $\text{Fe}_3\text{O}_4@\text{C}$ spines during multiple reflections.³⁴

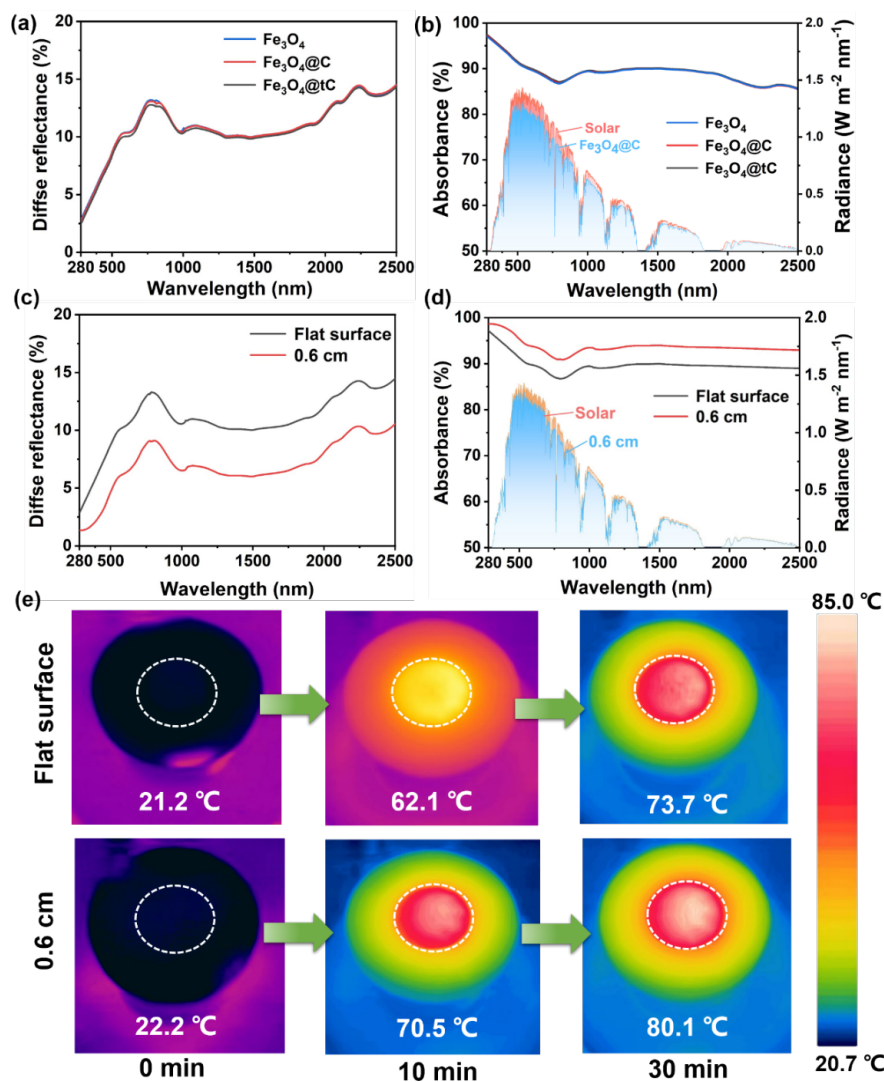


FIGURE 5 Diffuse reflection spectra of magnetic samples in the wavelength range of 280–2500 nm (a). AM 1.5 G solar spectrum and UV-Vis-NIR absorption spectra (b). Diffuse reflection spectra of the Fe₃O₄@C flat and photothermal layer formed by Fe₃O₄@C at 0.6 cm in the wavelength range of 280–2500 nm (c). AM 1.5 G solar spectrum and UV-Vis-NIR absorption spectra (d). The IR thermal images of magnetic evaporator under 1-sun illumination (e).

The low diffuse reflectance of photothermal layer corresponded to the higher light absorption with negligible transmittance. Sunlight absorptance in the range of 280–2500 nm was used to evaluate the photothermal evaporator, which was calculated as below:

$$\text{Sunlight absorptance} = \frac{\int_{280}^{2500} I(\lambda) \times A(\lambda) d\lambda}{\int_{280}^{2500} I(\lambda) d\lambda} \quad (1)$$

where $I(\lambda)$ is the sunlight intensity function at the wavelength (λ) from 280 to 2500 nm, $A(\lambda)$ is the absorptance of samples at the corresponding wavelength (Figure 5b-d). The sunlight absorptance of flat Fe₃O₄@C surface was around 89.6%. In comparison, the absorptance of spiny surface could be enhanced over 94.6% as the distance was 0.6 cm. Thanks to the high absorptance of sunlight, the photothermal layer formed by Fe₃O₄@C at a distance of 0.6 cm from magnet revealed high performance on the light-to-thermal conversion.

After being exposed to the simulated solar light ($\sim 1000 \text{ W m}^{-2}$) for 30 mins, spiny surface exhibited a higher surface temperature of surface up to $80.1 \text{ }^\circ\text{C}$ on average than the flat surface of just $73.7 \text{ }^\circ\text{C}$ (Figure 5e).

For testing convenience, the data was mainly collected from the center of the spiny surface. Adjusting the distance to the magnet, spiny surface showed changes in light harvesting. As the distances were 0.1 cm and 1.1 cm, the diffuse reflectances were similar to the result at 0.6 cm. While, as the distance enlarged to 1.6 cm, there was an obvious increase in diffuse reflectance, which was as high as $\sim 12 \%$ in visible region (Figure S7a-b).

During photothermal evaporation, the evaporator was wetted by water, and it was necessary to investigate the light absorption of photothermal layer in the wet state. After being wetted by water, the diffuse reflectances of all photothermal layers were further decreased (Figure S7c-d). This could be attributed to the presence of a thin water layer around the wettable $\text{Fe}_3\text{O}_4@\text{C}$ that optimized the optical path following the Fresnel equation.^{34,38}

2.4. Photothermal evaporation performance of magnetic photothermal evaporator

The photothermal evaporator for measurement was assembled as the inserted image in Figure 6a shown. Magnetic nanoparticles were located on a 3D-printed holder to form the photothermal layer. Between them, there was a piece of air-laid paper for water supply. To adjust the location of photothermal layer in magnetic field, a disc magnet was placed on the top of screw plug, which could be rotated to change the distance between the nanoparticles and magnet.

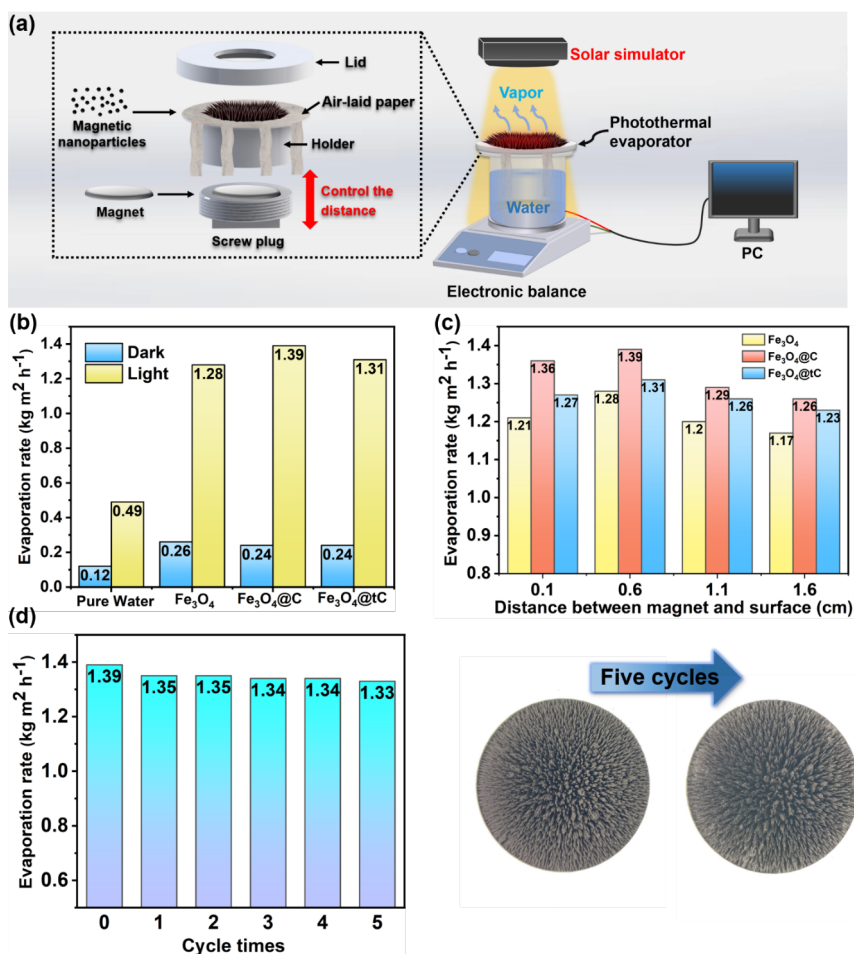


FIGURE 6 Schematic illustration of the fabrication of magnetic photothermal evaporator (left) and the evaporation test system (right) (a). The water evaporation rates of Fe_3O_4 , $\text{Fe}_3\text{O}_4@\text{C}$ and $\text{Fe}_3\text{O}_4@\text{tC}$ evaporators under dark and light conditions respectively (b). Water evaporation rates of photothermal evaporators at various distances between magnet to nanoparticles (c). The evaporation rate and the durability of magnetic evaporator (d). The images right showed the surface morphologies before and after five cycling experiments.

The performance of magnetic evaporator on water evaporation was been systematically evaluated based on a lab-made system that was composed of a solar simulator with a fixed light intensity of 1000 W m^{-2} and an electronic balance connected to PC (Figure 6a). Evaporation measurements were performed in a temperature and humidity chambers to minimize the effect of conditions. The set temperature and relative humidity were fixed at $25 \text{ }^\circ\text{C}$ and 50%, respectively.

The evaporation performances with the assistance of magnetic nanoparticles were shown in Figure 6b in comparison with the natural evaporation. The evaporation rates of pure water were $0.49 \text{ kg m}^{-3} \text{ h}^{-1}$ and $0.12 \text{ kg m}^{-3} \text{ h}^{-1}$ with and without light. As the distance was fixed at 0.6 cm, evaporators assembled in magnetic field accelerated the photothermal rates to 0.26, 0.24, $0.24 \text{ kg m}^{-3} \text{ h}^{-1}$ respectively in dark and 1.28, 1.39, $1.31 \text{ kg m}^{-3} \text{ h}^{-1}$ respectively under illumination. The higher evaporation rates of magnetic evaporators in dark could be attributed to the enlargement of evaporation interface area via spiny morphology. While, the good photothermal ability of magnetic spines resulted in faster water evaporation with light. Among the three kinds of nanoparticles, $\text{Fe}_3\text{O}_4@\text{C}$ showed the best performance on photothermal evaporation. Such result was consistent with the solar light absorptance data in Figure 5 and Figure S7.

The water evaporation performance could also be affected by the distance between the spiny surface and magnet. As discussed above, the magnetic field tended to be uniform at an appropriate distance. A relatively integral spiny surface could be assembled under the induction of magnetic field, even as the loading density of nanoparticles was as low as 1 mg mm^{-2} . For $\text{Fe}_3\text{O}_4@\text{C}$, the water evaporation rates could reach up to 1.36, 1.39, 1.29 and $1.26 \text{ kg m}^{-3} \text{ h}^{-1}$, as the distance was changed from 0.1 to 0.6, 1.1 and 1.6 cm. At a narrow distance, the coverage region with nanoparticles was incomplete under the non-uniform magnetic field. Exposed partial sites reduced the light harvesting even in wet state, which caused the lower evaporation rate. As the distance increased from 1.1 to 1.6 cm, the evaporation rate declined continuously because of the decay of magnetic field strength. A weak magnetic field could hardly remain the spiny morphology against the strong surface tension of water in wet state. Fe_3O_4 and $\text{Fe}_3\text{O}_4@\text{tC}$ showed a similar tendency for water evaporation at different distances to magnet.

Furthermore, to evaluate the stability of magnetic evaporator, the photothermal evaporation rates were measured under 12-hour illumination alternating with 12-hour darkness. After 5 cycles, the evaporation rate still kept up to about $1.33 \text{ kg m}^{-3} \text{ h}^{-1}$, which was 96% of the initial rate (Figure 6d). The stable performance on long-term photothermal evaporation could be attributed to the good stability of the spiny morphology of $\text{Fe}_3\text{O}_4@\text{C}$. Meanwhile, thanks to the protection of carbon layer, $\text{Fe}_3\text{O}_4@\text{C}$ remained the crystalline structure of Fe_3O_4 without obvious change which was confirmed by XRD in Figure 7e. In this case, the $\text{Fe}_3\text{O}_4@\text{C}$ layer could maintain its photothermal performance under long-term illumination for water evaporation, thus enabling low-cost actual water desalination.

2.5. Solar-driven desalination of magnetic photothermal evaporator

To evaluate the performance of magnetic evaporator on seawater, photothermal evaporation was measured with five concentrations of saline solutions to simulate seawater from different seas, including the Baltic Sea (0.8 wt%), the world ocean (3.5 wt%), the Red Sea (4.1 wt%) and the Dead Sea (30 wt%). As shown in Figure 7a, the evaporation rate under illumination decreased from $1.39 \text{ kg m}^{-3} \text{ h}^{-1}$ for DI water to 1.37, 1.31, 1.26 and $0.98 \text{ kg m}^{-3} \text{ h}^{-1}$ for the simulated seawater of the Baltic Sea, world ocean, the Red Sea and the Dead Sea, respectively. Correspondingly, the evaporation rate of evaporator decreased from 0.27 to 0.25, 0.19, 0.18 and $0.16 \text{ kg m}^{-3} \text{ h}^{-1}$, respectively in dark. The decrease in evaporation rate is due to the lower saturation vapor pressure of seawater. Higher concentration of saline solution indicated lower saturation vapor pressure, and further caused slower evaporation. The real seawater from Bohai Bay (obtained at $38^\circ 53' \text{N}$, $121^\circ 34' 34'' \text{E}$)

was also employed in measurement, and the evaporation rate with $\text{Fe}_3\text{O}_4@\text{C}$ evaporator was about $1.35 \text{ kg m}^{-3} \text{ h}^{-1}$ (Figure 7a).

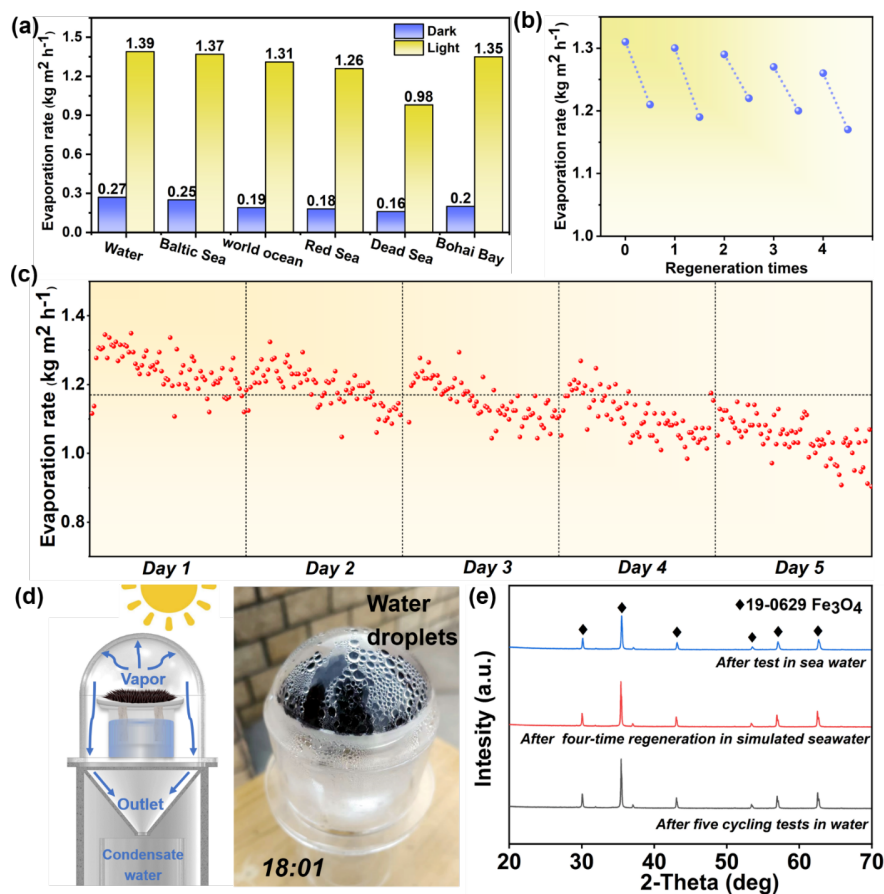


FIGURE 7 Water evaporation rates of magnetic evaporator for saline solutions with different concentrations and seawater from Bohai Bay under 1-sun illumination (a). The evaporation rates and the regeneration performance of magnetic evaporator in 8-hour evaporation for simulated seawater (b). Long-term seawater evaporation performance of magnetic evaporator 12-hour illumination alternating with 12-hour darkness, 3.5 wt% of saline solution was used as simulated seawater (c). Schematic diagram of condensate water collection device made of PMMA for outdoor solar-driven desalination (d). The XRD spectra of the $\text{Fe}_3\text{O}_4@\text{C}$ after photothermal evaporation in various conditions (e).

The stability of the evaporator in seawater evaporation was carefully measured as Figure 7b and Figure 7c shown. In Figure 7b, photothermal evaporation with the $\text{Fe}_3\text{O}_4@\text{C}$ evaporator was sustained for 8 hours. Thereafter, the evaporator was regenerated by washing it with a little water. During continuous evaporation, the evaporation rate for simulated seawater (3.5 wt%) gradually decreased from $1.31 \text{ kg m}^{-3} \text{ h}^{-1}$ at the beginning to $1.21 \text{ kg m}^{-3} \text{ h}^{-1}$ with the assistance of evaporator. The precipitation of salt crystals on spiny surface could be considered as the reason for the slight efficiency decline. By removing salt crystals through washing them in water, $\text{Fe}_3\text{O}_4@\text{C}$ nanoparticles could be collected and assembled into the spiny surface again for next measurement. After four-time regeneration, evaporator still showed an evaporation rate around $1.26 \text{ kg m}^{-3} \text{ h}^{-1}$ at the beginning, about 96% of the initial result. It was demonstrated that the magnetic field-induced method is an alternative reusable strategy to improve the cycling performance of evaporator.

In the other measurement as shown in Figure 7c, the $\text{Fe}_3\text{O}_4@\text{C}$ evaporator was continuously used for 12-hour evaporation under illumination and 12-hour regeneration by itself in dark, which simulated the case in daytime and nighttime. The evaporation rate was decreased from $1.30 \text{ kg m}^{-3}\text{h}^{-1}$ to $1.19 \text{ kg m}^{-3}\text{h}^{-1}$ with the accumulated salt crystals after 12-hour evaporation of simulated seawater (3.5 wt%). During the regeneration in dark, the salt crystals were not completely dissolved as Figure S8 shown, which might be due to the weak hydrophilicity of $\text{Fe}_3\text{O}_4@\text{C}$. Salt ions were difficult to diffuse rapidly into the bulk solution. Thus, the regeneration of evaporator was not sufficient. The evaporation rate on Day 5 was just about $1.12 \text{ kg m}^{-3} \text{ h}^{-1}$, which was 86% of the initial rate after four-time regeneration. The performance decline of evaporator could be attributed to the accumulation of crystalline salt that influenced the light harvesting. During the application in seawater, $\text{Fe}_3\text{O}_4@\text{C}$ still kept stable without an observable change in the crystal structure as XRD patterns shown in Figure 7e.

Furthermore, the outdoor experiment was conducted to investigate the potential of magnetic photothermal evaporator for practical application. The lab-made evaporator in above measurement had a small size which was not appropriate for practical desalination. Consequently, a larger magnet with a diameter of 60 mm was used to compose a larger evaporator. A portable water collection device made of polymethyl methacrylate (PMMA) was used for solar-driven desalination. The specific design of device was shown in Figure 7d. The as-prepared larger evaporator was placed inside the device and converted solar light to heat for vapor generation. The formed vapor condensed into water droplets that flowed along the side walls into the container located below. After actual solar irradiation in an open field from 07:35 to 18:06 (Sunset time) on March 14 ($38^\circ 53' 28''\text{N}$, $121^\circ 31' 31''\text{E}$) (Figure S9), over 10 ml of water was finally collected. Meanwhile, there was no visible salt precipitation on the black $\text{Fe}_3\text{O}_4@\text{C}$ layer. Suffering from the interference elements including low temperatures, clouds, condensed water droplets and PMMA cover, the actual light intensity accepted by sample was far lower than 1000 W m^{-2} . As Figure S10 shown, the concentrations of residual Na^+ , K^+ , Mg^{2+} , Ca^{2+} , Cl^- , Br^- and SO_4^{2-} in condensate water were down to about 30.54, 3.97, 1.95, 3.459, 41.52, 0.05 and 7.02 mg L^{-1} , respectively, which were all lower than the standard limits of desalinated water from WHO (World Health Organization).³⁹

3. Conclusion

In summary, we fabricated a magnetic field induced photothermal evaporator assembled by carbon-coated $\text{Fe}_3\text{O}_4(\text{Fe}_3\text{O}_4@\text{C})$ nanoparticles, which revealed the adjustable spiny surface structure corresponding to the relative distance to magnet. At an appropriate relative distance, just 1 mg mm^{-2} of $\text{Fe}_3\text{O}_4@\text{C}$ nanoparticles was necessary to form a well-distributed spiny surface. With the optimized surface structure, the solar absorbance of evaporator could reach up to 94.6% via multiple reflections. The $\text{Fe}_3\text{O}_4@\text{C}$ assembled evaporator obviously improved the water evaporation as high as $1.39 \text{ kg m}^{-2}\text{h}^{-1}$ under the 1-sun illumination, about 2.8 times higher than natural evaporation. Meanwhile, the magnetic evaporator could also accelerate the seawater evaporation up to $1.31 \text{ kg m}^{-2} \text{ h}^{-1}$ with just a little performance degradation during long desalination owing to the good stability of $\text{Fe}_3\text{O}_4@\text{C}$. The work can be considered as a beneficial attempt to optimize the magnetic evaporator for application. Besides, the facile adjustment of the magnetic nanoparticles assembled surface via the position in magnetic field has high potential in not only sustainable solar-driven fresh water generation but more fields of water treatment.

Experimental Section

Preparation of the carbon-coated nanoparticles : The carbon-coated nanoparticles were synthesized by a typical hydrothermal method. Specifically, 0.3 g of Fe_3O_4 nanoparticles, 1 mL of acrylic acid, and 40 mL of H_2O were mixed with a certain amount of glucose in a 100 mL capped glass bottle. Different amounts of glucose led to different thicknesses of carbon layers around Fe_3O_4 nanoparticles. The mixture was stirred vigorously at room temperature for 4 h and transferred to a 100 mL Teflon-lined stainless-steel autoclave. The autoclave was heated at 200 for 12 h, then naturally cooled to room temperature at the end of the reaction. The black products were washed with DI water and anhydrous ethanol alternately three times. Subsequently, the products were dried at 60 degC for 6 h. The obtained samples were named $\text{Fe}_3\text{O}_4@\text{C}$, and $\text{Fe}_3\text{O}_4@\text{tC}$ respectively according to 1.0 g/2.0 g of glucose.

Fabrication of magnetic photothermal evaporator : A 3D model of the evaporator was established by SOLIDWORKS software and was converted into object through 3D printer (raise3D Pro2 Plus) using PLA (polylactic acid) wire. This evaporator had two parts including an upper holder to support the magnetic nanoparticles and a lower screw plug equipped with a NdFeB magnet. The distance between magnet and magnetic nanoparticles could be adjusted by rotating the screw plug. The air-laid paper was cut into a specific shape serving as water transfer channels. Magnetic nanoparticles were deposited at the holder at the density of 1 mg mm^{-2} , which could self-assemble into a spiny surface induced by magnetic field.

Supporting Information

Supporting Information is available from the Wiley Online Library or from the author.

Acknowledgements

This work was funded by the Fundamental Research Funds for the Central Universities (DUT22GF306, DUT22LAB607), Dalian Science and Technology Innovation Fund (2022JJ13SN098), the Natural Science Foundation of Liaoning Province (2022-MS-144) and Project 1912 Funds provided by the Chinese Aeronautical Establishment.

The authors declare no potential conflict of interest.

Received: ((will be filled in by the editorial staff)) Revised: ((will be filled in by the editorial staff)) Published online: ((will be filled in by the editorial staff))

References

1. Ghazi ZM, Rizvi SWF, Shahid WM, Abdulhameed AM, Saleem H, Zaidi SJ. An overview of water desalination systems integrated with renewable energy sources. *Desalination* 2022; 542: 116063.
2. He F, Wu XC, Gao J, Wang ZX. Solar-driven interfacial evaporation toward clean water production: burgeoning materials, concepts and technologies. *J Mater Chem A* 2021; 9: 27121-27139.
3. Ahmed FE, Hashaikeh R, Hilal N. Solar powered desalination—Technology, energy and future outlook. *Desalination* 2019; 453: 54-76.
4. Wang YC, Sun XY, Tao SY. Rational 3D Coiled Morphology for Efficient Solar-Driven Desalination. *Environ Sci Technol* 2020; 54 (24): 16240-16248.
5. Gao MM, Peh CK, Meng FL, Ho GW. Photothermal Membrane Distillation toward Solar Water Production. *Small Methods* 2021; 5 (5): 2001200.
6. Wang YD, Hu JQ, Yu L, Wu X, Zhang YY, Xu HL. Recent strategies for constructing efficient interfacial solar evaporation systems. *Nano Res Energy* 2023; 1: 1-19.
7. Tao P, Ni G, Song CY, et al. Solar-driven interfacial evaporation. *Nat Energy* 2018; 3: 1031-1041.
8. Chen GY, Sun JM, Peng Q, Sun Q, et al. Tang B. Z. Biradical-Featured Stable Organic-Small-Molecule Photothermal Materials for Highly Efficient Solar-Driven Water Evaporation. *Adv Mater* 2020; 32 (29): 1908537.
9. Mascaretti L, Schirato A, Zbořil R, et al. Solar steam generation on scalable ultrathin thermoplasmonic TiN nanocavity arrays. *Nano Energy* 2021; 83: 105828.
10. Bu YM, Zhou YH, Lei WW, et al. A bioinspired 3D solar evaporator with balanced water supply and evaporation for highly efficient photothermal steam generation. *J Mater Chem A* 2022; 10: 2856-2866.
11. Chen ZC, Li Q, Chen XM. Porous Graphene/Polyimide Membrane with a Three-Dimensional Architecture for Rapid and Efficient Solar Desalination via Interfacial Evaporation. *ACS Sustainable Chem Eng* 2020; 8 (36): 13850-13858.

12. He MT, Dai HY, Liu HJ, et al. High-Performance Solar Steam Generator Based on Polypyrrole-Coated Fabric via 3D Macro-and Microstructure Design. *ACS Appl Mater Interfaces* 2021; 13 (34): 40664-40672.
13. Zhang XY, Ren LP, Xu J, Shang B, Liu X, Xu WL. Magnetically Driven Tunable 3D Structured Fe₃O₄ Vertical Array for High-Performance Solar Steam Generation. *Small* 2022; 18 (5): 2105198.
14. Wang YC, Wang CZ, Song XJ, Megarajan SK, Jiang HQ. A facile nanocomposite strategy to fabricate a rGO-MWCNT photothermal layer for efficient water evaporation. *J Mater Chem A* 2018; 6: 963-971.
15. Yin, Z, Wang HM, Jian MQ, et al. Extremely Black Vertically Aligned Carbon Nanotube Arrays for Solar Steam Generation. *ACS Appl Mater Interfaces* 2017; 9 (34): 28596-28603.
16. Zhou, L, Tan, YL, Ji, DX, et al. Self-assembly of highly efficient, broadband plasmonic absorbers for solar steam generation. *Sci Adv* 2016; 2 (4): 1501227.
17. Qiu PX, Liu FL, Xu CM, et al. Porous three-dimensional carbon foams with interconnected microchannels for high-efficiency solar-to-vapor conversion and desalination. *J Mater Chem A* 2019; 7: 13036-13042.
18. Yao HZ, Zhang PP, Yang C, et al. Cheng H. Janus-interface engineering boosting solar steam towards high-efficiency water collection. *Energy Environ Sci* 2021; 14: 5330-5338.
19. Ai S, Ma M, Chen YZ, Gao XH, Liu G. Metal-ceramic carbide integrated solar-driven evaporation device based on ZrC nanoparticles for water evaporation and desalination. *Chem Eng J* 2022; 429: 132014.
20. Liu, WD, Kappl M, Steffen W, Butt HJ. Controlling supraparticle shape and structure by tuning colloidal interactions. *J Colloid Interface Sci* 2022; 607: 1661-1670.
21. Liu, WD, Kappl M, Butt HJ. Tuning the Porosity of Supraparticles. *ACS Nano* 2019; 13 (12): 13949-13956.
22. Chen, R, Wu ZJ, Zhang TQ, Yu TC, Ye MM. Magnetically recyclable self-assembled thin films for highly efficient water evaporation by interfacial solar heating. *RSC Adv* 2017; 7: 19849-19855.
23. Li DS, Chen Q, Chun J, Fichthorn K, Yoreo JD, Zheng HM. Nanoparticle Assembly and Oriented Attachment: Correlating Controlling Factors to the Resulting Structures. *Chem Rev* 2023; 123 (6): 3127-3159.
24. Yang Y, Xu GY, Huang SF, Yin YG. Experimental study of the solar-driven interfacial evaporation based on a novel magnetic nano solar absorber. *Appl Therm Eng* 2022; 217: 119170.
25. Ni K, Wang ZZ. Recent Progress on the Development of Magnetically-Responsive Micropillars: Actuation, Fabrication, and Applications. *Adv Funct Mater* 2023; 33 (14): 2213350.
26. Dai ZY, Chen G, Ding S, et al. Facile Formation of Hierarchical Textures for Flexible, Translucent, and Durable Superhydrophobic Film. *Adv Funct Mater* 2020; 31 (7): 2008574.
27. Yang F, Chen JX, Ye ZY, Ding DW, Myung NV, Yin YD. Ni-based Plasmonic/Magnetic Nanostructures as Efficient Light Absorbers for Steam Generation. *Adv Funct Mater* 2020; 31 (7): 2006294.
28. Hu YJ, Ma HY, Wu MM, et al. A reconfigurable and magnetically responsive assembly for dynamic solar steam generation. *Nat Commun* 2022; 13: 4335.
29. Zhou Q, Ji B, Hu B, et al. Tilted magnetic micropillars enabled dual-mode sensor for tactile/touchless perceptions. *Nano Energy* 2020; 78: 105382.
30. Li DK, Huang JX, Han GC, Guo ZG. A facile approach to achieve bioinspired PDMS@Fe₃O₄ fabric with switchable wettability for liquid transport and water collection. *J Mater Chem A* 2018; 6: 22741-22748.
31. Kang M, Seong M, Lee D, Kang SM, Kwak MK, Jeong HE. Self-Assembled Artificial Nanocilia Actuators. *Adv Mater* 2022; 34 (24): 2200185.

32. Yi SZ, Wang J, Chen ZP, et al. Cactus-Inspired Conical Spines with Oriented Microbarbs for Efficient Fog Harvesting. *Adv Mater Technol* 2019; 4 (12): 1900727.
33. Song YY, Yu ZP, Dong LM, et al. Cactus-Inspired Janus Membrane with a Conical Array of Wettability Gradient for Efficient Fog Collection. *Langmuir* 2021; 37 (46): 13703-13711.
34. Wang YC, Tang B, Han P, et al. Adjustable photothermal device induced by magnetic field for efficient solar-driven desalination. *EcoMat* 2021; 3 (5): 12139.
35. Cornell RM, Schwertmann U. *Iron Oxides: Structure, Properties, Reactions, Occurrences and Uses*. New York: John Wiley & Sons; 2003.
36. Hima HI, Xiang X, Zhang L, Li F. Novel carbon nanostructures of caterpillar-like fibers and interwoven spheres with excellent surface super-hydrophobicity produced by chemical vapor deposition. *J Mater Chem* 2008; 18: 1245-1252.
37. Nofuentes G, García-Domingo B, Muñoz JV, Chenlo F. Analysis of the dependence of the spectral factor of some PV technologies on the solar spectrum distribution. *Appl Energy* 2014; 113: 302-309.
38. Shi Y, Li RY, Shi L, Ahmed E, Jin Y, Wang P. A Robust $\text{CuCr}_2\text{O}_4/\text{SiO}_2$ Composite Photothermal Material with Underwater Black Property and Extremely High Thermal Stability for Solar-Driven Water Evaporation. *Adv Sustain Syst* 2018; 2 (3): 1700145.
39. WHO. Safe Drinking Water from Desalination. <https://www.who.int/publications/i/item/WHO-HSE-WSH-11.03>. 2020.

The table of contents

A magnetic field induced photothermal evaporator assembled by carbon-coated Fe_3O_4 ($\text{Fe}_3\text{O}_4@\text{C}$) nanoparticles, which revealed the adjustable surface structure corresponding to the relative distance to magnet. The optimized evaporator assembled by $\text{Fe}_3\text{O}_4@\text{C}$ showed a uniform spiny surface contributing to an obvious improvement on evaporation rate under illumination and lower performance degradation in long-term desalination.

Keywords

photothermal evaporation, desalination, carbon-coated magnetic nanoparticles, magnetic field induced, adjustable surface structure

M. Zhou, P. Han, G. Qi, D. Gao, H. M. Abdel-Ghafar, Y. Wang* and S. Tao*

Magnetic Field Induced the Assembling of Photothermal Evaporator for Efficient Solar-driven Desalination

ToC figure

